8-1-1994

Energy Deposition and K-Shell Ionization of Supernovae

Lih-Sin The
Clemson University

William T. Bridgman
Clemson University

Donald D. Clayton
Clemson University, claydonald@gmail.com

THE ASTROPHYSICAL JOURNAL SUPPLEMENT SERIES, 93:531–548, 1994 August

ENERGY DEPOSITION AND K-SHELL IONIZATION OF SUPERNOVAE

LIH-SIN THE, WILLIAM T. BRIDGMAN, AND DONALD D. CLAYTON
Department of Physics and Astronomy, Clemson University, Clemson, SC 29634-1911
Received 1991 July 17; accepted 1994 January 10

ABSTRACT

We present explicit evaluation of K-shell ionization caused by photoelectric absorption, by Compton scattering, and by electron collisions in supernovae envelopes. Each process derives from the radioactivity that dominates the bolometric luminosity of the model supernovae. We include the ionization by bremsstrahlung. We find that electron-collision ionization with decelerating Compton electrons is the dominant process of K-shell ionization for light elements (lighter than Si) whereas photoelectric K-shell absorption of Comptonized gammas is the dominant process of K-shell ionization for heavy elements (like Fe). The relative importance of the ionization processes also depends upon composition and upon time, as well as upon supernova type. For Type Ia all four ionization sources are of importance. We present fitting formulas for the deposition of radioactive power in each class of models studied. The energy deposition of all mechanisms decreases with time, including the rate of K-shell ionizations of all elements throughout the supernovae model evaluated herein. We compare the relative contributions to the energy deposition and confirm with greater numerical detail results already established.

Subject headings: gamma rays: theory — radiation mechanisms: nonthermal — stars: individual (SN 1987A) — stars: interiors — supernovae: general

1. INTRODUCTION

This work contributes to the attempt to understand the energy deposition mechanisms, structure, and distribution of matter in supernovae. Owing to our interest in X- and γ-ray astronomy, we focus on the K-shell ionization rate of major elements and on the relative importance of the physical processes responsible for it. Measurements over a wide range of the electromagnetic spectrum from SN 1987A have presented an opportunity to study the inner debris of a supernova in more detail. The detection of ^{56}Co gamma lines from SN 1987A provided conclusive evidence that that radioactive nucleus is produced abundantly in supernovae, a confirmation long hoped for (Clayton, Colgate, & Fishman 1969). These radioactive gamma photons fuel the supernova light curve and are the source of nonthermal energy responsible for almost all energetic processes and radiation after the explosion. As the radioactive nuclei decay, most of the gamma-ray energy is deposited at early times into the ejecta envelope by Compton scattering and by photoelectric absorption, producing the X-ray and gamma-ray lines and the gamma-ray continuum of supernovae. As the ejecta expands and becomes more transparent, more of the primary radiation can escape, but at the same time other processes caused by its energy deposition, such as atomic ionization, infrared and ultraviolet lines, and molecular formation become more evident. One such interesting aspect of supernovae is the primary topic of this paper, namely inner-shell ionization of matter, especially of atomic K shells, and the K X-ray fluxes that result. With a Monte Carlo code we are able to follow the degradation of the gamma ray energy and to describe the relative importance of differing physical processes to K-shell ionization.

McCray, Shull, & Sutherland (1987) predicted the emergence of X-rays, UV emission lines, and continuum before the observed detection of SN 1987A. In their model, the Comptonized soft X-rays ($\sim$30 keV) are deposited in the envelope and excite or ionize matter in the envelope that produces the IR, UV, and soft X-ray photons. Axelrod (1980) described most of the relevant processes in his Ph.D thesis. These are nonthermal processes unrelated to states of thermal equilibrium. For example, Graham (1988) attributed the growth of the prominent features of He I 1.083 μm in the infrared spectrum of SN 1987A (Elias et al. 1988) from 1987 May (t = 76 d) to July (t = 135 d) to the ionization by ^{56}Co decay gamma rays. Infrared spectra calculated by Colgan & Hollenbach (1988) and by Fransson & Chevalier (1989) have used gamma-ray energy deposition as a source of ionization; they conclude that the late IR spectrum is a good diagnostic of supernovae structure. In detailed calculations Fransson & Chevalier (1989), Swartz (1991), Kozma & Fransson (1992), and Eastman & Pinto (1993) describe how the energy transfer from gamma rays to electrons is fed into the ionization balance equation between ion i and $i + 1$ to calculate the relative abundances of ions, and thus of emission lines of ions. The emphasis within those clarifying works has lain on radiative transfer and the intensities of optical, infrared, and ultraviolet transitions. We choose instead to emphasize the K X-ray emission because those lines reflect more directly the early stages of the nonthermal energy cascades following Compton scattering. In this paper we repeat some of these earlier findings concerning energy deposition with greater numerical detail, and do so within explicit numerical models of differing supernova types.

We will calculate the K-shell ionization rate of elements in the ejecta for different types of supernova in considerable detail because K X-rays may be the most unambiguous diagnostic of the non-LTE state of matter, although they are, of course, harder to detect than IR and optical lines. Our explicit calculations clarify the relative significance of differing ionization mechanisms for the K shells of different major elements. Emphasis in other studies has been on outer-shell ionization, be-

cause that rate governs the free-electron density. Many of these studies have been without a specific numerical supernova model. Our concentration on K-shell ionization reflects primarily our interest in high-energy astronomy, where the resulting fluorescence can provide unique detectable diagnostics. We therefore use explicit K-ionization processes within distinct numerical models for several supernova types. The K-shell photoionization and Compton ionization are calculated explicitly with a Monte Carlo gamma-ray transport code (The, Burrows, & Bussard 1990) that follows the down-scattering of gamma rays from ^{56}Co. The energy spectra of Compton and photoelectric electrons are recorded, and their subsequent collisional ionization of K-shell electrons during their deceleration is also calculated. It is this last aspect, the collisional history of the energetic electrons, that is the new aspect of our calculations.

We include in our analysis the ionization by bremsstrahlung created during the deceleration of Compton electrons. Clayton & The (1991, hereafter CT) recently introduced and calculated this particular by-product of the very large energy stored in Compton electrons, and they found that bremsstrahlung luminosity dominates the supernova emission below 20 keV or so and that this bremsstrahlung emission can also be used as a diagnostic tool for determining the mixing in the ejecta. Their explicit calculation of the fast-electron spectrum is the starting point for the subsequent effects of those electrons. We calculate here collisional K-ionization rates by those electrons, whose spectra we recalculate for several models. The limitations of our calculation and results are discussed in § 2.

It seems unclear to many investigators which mechanism (photoionization or electron impact) is the more likely mechanism of ionization. It is our objective to show the significance of each mechanism for the K ionization rate of several elements at different locations and at different times in the ejecta of different types of supernovae. A separate external mechanism that has been discussed by other investigators (but not evaluated here) for SN 1987A is the photoionization by soft X-rays created during the interaction of the supernova ejecta with circumstellar matter. We do our computation for two models of SN 1987A (W10hmm of Pinto & Woosley 1988a, b and SN11E1 of Nomoto et al. 1988; Kumagai et al. 1989), for one model W7 (Nomoto, Thielemann, & Yokoi 1984) of a Type Ia, and one of a He-core model WR6C (Ensman & Woosley 1988) of a Type Ib as well as for fully mixed versions of W7 and of WR6C. The optical light curves, X-ray continuum, and gamma-ray line fluxes of these models have been evaluated by many investigators (Pinto & Woosley 1988a, b; Nomoto et al. 1988; Kumagai et al. 1989; Burrows & The 1990; The, Clayton, & Burrows 1991; CT) and have been used as diagnostic tools to determine the structure, mixing, and progenitor of supernovae. Our mixed models remain spherically symmetric; therefore, they do not evaluate the effect of inhomogeneities. We record separately the K-shell ionizations caused by photoelectric absorption, Compton scattering, collisions of recoil electrons during their stopping, and bremsstrahlung in order to clarify their relative importance. We believe these results provide additional insight into physical processes in the interiors of supernovae and may in many cases be directly observable as K-shell emission lines. In § 2 we explain the models and the method of our calculation. In § 3 we present our results of K-shell ionization of each element as they are distributed in the ejecta and as it evolves with time for different types of supernovae, and also of the external fluxes of strong K X-rays. The last section contains discussion and conclusions.

2. METHODS OF CALCULATION

The gamma-ray transport algorithm for Monte Carlo simulation used in our computation has been presented in detail by The et al. (1990) and Podznyakov, Sobol, & Sunyaev (1983). We improve the statistics of the gamma-ray transport code by splitting each photon beam of energy below 100 keV into five beams of photons. We thereby increase the number of trials by a factor of 5 for photons with energy below 100 keV. This increases the accuracy for low-energy photons, which are severely depleted by photoelectric absorption. In this calculation we not only follow the photons' scatterings and absorptions, we also record where and how the photons interact with matter in the ejecta. We thereby construct the distribution of K-shell vacancies in the envelope as function of atomic nuclei, time evolution, and radial mass distribution of the ejecta. Following their creation during radioactive ^{56}Ni and ^{56}Co decay, most gamma photons are Compton scattered before they escape or are photoelectrically absorbed. Since the energies of these photons are much larger than the binding energy of electrons in atoms, scatterings can be modeled as Compton scatterings on free electrons, and if the kinetic energy of the electron after such a free scattering is larger than the binding energy of the electron in the atom, the scattering creates a vacancy in a shell of the atoms. To carry out such a calculation we let a random number choose the bound electron that is ejected. We record the K-shell vacancies of each element that are created by scatterings, photoelectric absorption of photons, ^{56}Fe K-vacancies created directly by electron capture by the ^{56}Co nucleus, and inelastic electrons.

For the electron effects we begin with the Compton electron spectra from each zone of the ejecta envelope. The Compton-recoil spectrum has been calculated by CT, and it follows an energy-break power law $(1 + E/E_o)^{-\alpha}$; for example, for Type II model $\alpha = 2$ and E_o evolves from 16 to 21 keV from day 175 to day 700, whereas for Type Ia (model W7), $\alpha \simeq 2.5$ and E_o evolves from 100 to 170 keV from day 20 to day 80. These initial spectra are used to calculate the K-shell ionization due to collisions of these electrons with atoms. These energetic electrons also produce bremsstrahlung during their deceleration (CT); we take the bremsstrahlung emission of each zone as an additional photon source and calculate the K-shell ionization and the K X-ray fluxes resulting from their interactions. Our objective is increased understanding of the relative contribution of each of these four processes to the K-shell vacancy rates. The ^{56}Co radioactivity creates K vacancies of Fe directly, because 81% of those decays occur by electron capture. We derive the relative rates of K, L, and other-shell electron captures from the calculation of Brysk & Rose (1955) as given in Wapstra, Nijgh, & Van Lieshout (1959) and Lederer & Shirley (1978). K vacancies created by photoelectric absorption, Compton scattering, and electron capture will clearly be followed by a standard probability of K and L X-ray emission.

2.1. *K-Shell Photoionization*

Photoelectric ionization becomes more important at low X-ray energies. Every photoelectric absorption of a photon having energy larger than the K-shell binding energy is assigned by a random number to either K-shell or L-shell ionization. For the purpose of this test only, we take the analytical formula for the ratio of K-shell and L-shell photoelectric cross sections from Hall (1936),

$$\frac{\tau_K}{\tau_L} = 8\left(\frac{Z - s_K}{Z - s_L}\right)^6 \{[1 + 4/3(E/E_K - 1)] \exp\{8(E/E_L - 1)^{-1/2} \times \tan^{-1}(E/E_L - 1)^{1/2} - 4\}\}[1 + 6E_L/E + 8(E_L/E)^2]^{-1}, \quad (1)$$

where Z is the atomic number, s_K and s_L are the screening constants of the K shell and L shell, respectively, and E_K and E_L are the ionization energies of the K shell and L shell, and E is the photon energy with $E > E_K$.

Each K-shell vacancy (due to absorption or scattering) after being recorded is followed by the possibility of K X-ray fluorescence that also mostly creates L vacancies and therefore L X-ray fluorescence. The number of K X-ray photons is obtained by multiplying the number of K-shell vacancies by the K-shell fluorescence yields, ω_K, of the absorbing atom. We take the fluorescence yields ω_K and ω_L from Table III.IV and Table IV.XII of Bambyneck et al. (1972). The scattering of this primary K X-ray is then followed until it is photoelectrically absorbed or escapes. In order to improve the statistics of escaping K X-ray fluxes, which might otherwise be poor due to the small number of photons, we simulate the emission histories such that the number of K X-ray emissions is set at 10 times the number of events creating K-shell vacancies. At the end, of course, we must divide by the same factors. In simulating the K X-ray emission, we inject the photon isotropically. Each scattering of this primary K X-ray photon can also create a secondary K-shell vacancy in a lighter element having lower K-shell binding energy (which is also recorded); the secondary K X-ray created by scattering or absorption is then followed only to determine if it escapes, so its absorption during creation of yet another (tertiary) K-shell vacancy (necessarily in a lighter element) is not recorded. This limited cascade simulation causes our estimated K-shell vacancies or K X-ray fluxes of elements lighter than Ar or S to be slightly underestimated. We can ignore this inaccuracy by evaluating the maximum possible error. The maximum error happens when the primary K X-ray of iron with $\omega_K \sim 0.34$ is absorbed by the next lighter abundant element, which in W10hmm is Ca with $\omega_K \sim 0.16$; therefore the omission of tertiary K-shell vacancies created by the K X-ray of Ca is $\sim 0.34 \times 0.16$ of iron K-shell vacancies. However, we shall see in the discussion below that the K-shell vacancy rate of this same light element created by inelastic electron scatterings is much larger than this maximum error; therefore the error in neglecting tertiary K photoelectric vacancies is negligible.

L-shell vacancies are also created, either by photoelectric absorption or following Auger and radiative transitions to K-shell vacancies. We simulate the L-shell absorption and L X-ray emission by taking the energy level and transition of each element from Zombeck (1990) and the probability of sublevel L photoelectric absorption from equations. (11) and (12) of Hall (1936) and from equations (45) and (46) of Gavrila (1961). For simplicity in our calculation, the ratio of transition probabilities between sublevel M_1 to $L_{2,3}$ and $M_{4,5}$ to $L_{2,3}$ is taken from the Table of Transition Probabilities for the Hydrogen Atom of Sobelman (1979). Auger and radiative transition to fill K-shell vacancies create L-shell vacancies; the relative number of each L-shell, their total, and L-shell fluorescence yields are obtained from Bambyneck et al. (1972). The subsequent scattering of this L X-ray is also simulated with 10 times the weight of events creating L-shell vacancies until it is absorbed; and although the secondary K X-ray vacancy created by the primary L X-ray is recorded, the secondary photons are followed only to calculate their emergent flux. We can again neglect the error by the same argument as in the above paragraph.

We have not included ionizations produced by low-energy Auger electrons (nonradiative transitions) that accompany the filling of shell vacancies. We utilize only electrons that are energized directly by Compton scattering since these electrons store vastly more nonthermal energy than do electrons from other processes. We also neglect ionizations and transitions of energy levels higher than L-shell, including the recombination process. Therefore our results on the number of K-shell vacancies somewhat underestimate the actual number. This error is greater for light elements than for heavy elements (especially for elements lighter than oxygen). We estimate the magnitude of inaccuracy of our calculated K-shell vacancies owing to this neglect of shells above L-shell as following: the number of vacancies of shells above K-shell is $\sim(Z - 2)/2$ times the number of K-shell vacancies. These vacancies do not create high fluxes of shell X-rays since the fluorescence yields of these shells are about two orders of magnitude lower than the fluorescence yield of K-shell; that is, for ^{56}Fe, $\omega_L \approx 1/228 \times \omega_K$, and for higher shells the differences are even larger.

To ensure that our results on K X-ray fluxes are not erroneous, we also run the radiation transport code with a slightly different procedure, taking the product of the number of K-shell vacancies and ω_K as the input source of K X-rays. The smoothness of the K-vacancy rate curves (Figs. 11–16) shows the adequate photon statistics in our gamma-ray transport simulation. We distribute the K X-ray source uniformly in the corresponding zone and emit the K X-rays isotropically. In Tables 3–7 we list some of the strongest K X-ray fluxes emerging from the surfaces of the models. The difference of K X-ray fluxes between the full gamma-transport code and the K-shell vacancies K X-ray transport is less than 20%.

Bremsstrahlung emission from outer supernova shells has been shown by CT to be the major process of surface X-ray escape below 20 keV; however, the K X-ray lines can be seen easily as strong emission lines below 7 keV. To assist the reader in understanding relative magnitudes, consider as a thought experiment the passage of one thousand 70 keV electrons through a sample of pure terrestrial iron. A K-vacancy in iron can produce an X-ray of about 6.4 keV. Then compare the number of photons produced by filling the K vacancies to the number of bremsstrahlung photons produced in the 5–7 keV energy range surrounding that line. To do this, first consider the production of bremsstrahlung. From the ICRU Report 37,

we find the radiation yield as 2.35×10^{-3} keV of bremsstrahlung per keV of electrons. Thus one thousand 70 keV electrons produces 164 keV of bremsstrahlung energy. To calculate how many of these photons have about 6 keV of energy, we look at the 5–7 keV energy range. The bremsstrahlung spectrum varies with $E^{-1.3}$ in the envelope (CT). As a result, the power spectrum varies as $E^{-0.3}$, and we find that in the energy range from 1 to 70 keV (the range of interest over which 70 keV electrons would emit bremsstrahlung), 4.4% of the energy (7.2 keV) is in the 5–7 keV band. To estimate the number of K-vacancies produced collisionally by the same 1000 electrons, we take the iron medium to have density of 7.87 g/cc which has 8.5×10^{22} atoms/cc. The number of K-vacancies is estimated with K-ionization cross section $\sigma^{\rm K} = 3 \times 10^{-22}$ cm^2 in terrestrial iron to be

$$\frac{dn_i^{\rm K}}{dx} = N_i \sigma_i^{\rm K} = (8.5 \times 10^{22}\ {\rm cm}^{-3})(3 \times 10^{-22}\ {\rm cm}^2) = 25 \text{ per electron per cm} . \quad (2)$$

The ICRU report gives a 70 keV electron a range of 1.5×10^{-3} cm in iron. Traveling this range (and dividing by two to approximate roughly the energy decrease over the range), 1000 electrons will generate a total of 19 K-vacancies. The K X-ray fluorescence yield of iron is about 0.34 yielding 5.7 K X-rays from the K-vacancies. These 6 keV photons give a total of 34.2 keV, 5 times the amount of energy emitted in bremsstrahlung between 5 and 7 keV, so we expect K-vacancy filling from electron collisions to dominate bremsstrahlung in the envelope within this narrow energy band.

We calculate the K-shell ionization and K X-ray escapes resulting from photoelectric absorption of bremsstrahlung by taking the bremsstrahlung spectrum of each zone from CT as input to our radiation transport code. Hereafter we will refer the K-shell photoelectric ionization by the Comptonized gammas (and by subsequent K and L X-rays) as the "K-shell photoelectric ionization" and the K-shell Compton scattering of Comptonized gammas as the "K-shell Compton scattering"; the total K-shell ionization by bremsstrahlung photons, including both photoelectric absorption and Compton scattering, is referred to as the "K-shell bremsstrahlung ionization." Our results will show that bremsstrahlung accounts for about 3%–5% of K-shell ionization of Si in Type I and Type II supernovae. In Type I supernovae, bremsstrahlung accounts for about 10%–20% of Fe K-shell ionization rate.

2.2. *K-Shell Electron-Collision Ionization*

The spectrum and rate of the energetic-electron production at each zone within the supernova interior resulting from Compton scattering and photoelectric absorption in the Monte Carlo gamma-ray transport simulation have been discussed in detail by CT. They used the electron spectrum to calculate the bremsstrahlung emitted during the stopping of each electron, whereas we use the energetic electron as as source of K-shell ionization while it collides and decelerates within the plasma.

The total number of K-shell vacancies per unit volume created in a species i, $n_i^{\rm K}$, while an electron decelerates from an initial kinetic energy T_i down to zero is given by the integral:

$$n_i^K = N_o \rho \frac{X_i}{A_i} \int_{T_i}^{0} \frac{\sigma_i^{\rm K}}{(dE/dx)}\, dT , \quad (3)$$

where X_i is the mass fraction of species i, A_i is the atomic mass of species i, ρ is the mass density of the medium, $\sigma_i^{\rm K}$ is the collision cross section for creating a K-vacancy, and N_o is Avogadro's number. The average linear energy loss in a medium of mixed composition is determined by a weighted average of the energy loss in the elementally pure media:

$$(dE/dx) = \sum_{i=1} X_i (dE/dx)_i , \quad (4)$$

where the summation runs over the different components of the medium and $(dE/dx)_i$ is the energy loss within a pure medium of species i given by (Rohrlich & Carlson 1954; ICRU Report 37, 1984)

$$(dE/dx)_i = -2\pi r_e^2 mc^2 N_o \rho \left(\frac{Z}{A}\right)_i \frac{1}{\beta^2} \times \left[\ln\left(\frac{T}{I_{\rm avg}}\right)^2 + \ln\left(1 + \frac{\tau}{2}\right) + F^-(\tau) - \delta\right] \quad (5)$$

where T is the electron kinetic energy, m is the electron rest mass, r_e is the classical electron radius, and $\beta = v/c$. The quantity $I_{\rm avg}$ is the average ionizing energy yielded to electrons liberated from the element by inelastic interactions with electrons (sometimes called the mean excitation energy). The function

$$F^-(\tau) = (1 - \beta^2)[1 + \tfrac{1}{8}\tau^2 - (2\tau + 1)\ln 2] \quad (6)$$

collects the terms of the energy loss for electrons that differ from the result for positrons (Rohrlich & Carlson 1954). The parameter τ is the dimensionless kinetic energy $\tau = T/mc^2$. The additive term δ is called the density correction factor. It is present due to the polarized wave that the passage of the electron produces in the surrounding medium (which in turn alters the electromagnetic fields acting on the electron). This effect is strong in dense media, but it can be ignored in the low-density medium expected in the supernova envelope, especially at times late enough to expect some K X-rays to be able to emerge.

For the collisional K-ionization cross section we used a semiclassical formula. A derivation of this cross section was included in Bates (1962). It contains two parts. The first part involves treating the ionization process as a classical electrostatic interaction, which gives the cross section as

$$\sigma^{\rm K}_{\rm classical} = 4n\left(\frac{I_{\rm H}}{I}\right)^2 \left(\frac{I}{T}\right)\left(1 - \frac{I}{T}\right)\pi a_o^2 , \quad (7)$$

where $I_{\rm H}$ is the binding energy of atomic hydrogen, I is the separation energy of the K shell of the atom, T is the kinetic energy of the incident electron, a_o is the Bohr radius, and n is the number of electrons in the K shell. The second part of the derivation uses a quantum mechanical calculation for specific elements to derive an approximate relation between the quan-

tum mechanical cross section and the classical cross section

$$\sigma^{K}_{quantum} = 1.3\sigma^{K}_{classical} \log_{10}\left(\frac{T}{I}\right), \quad (8)$$

where the leading constant 1.3 has been obtained by comparing the calculated cross section with the experimental results obtained for helium (Seaton 1962; Schram 1965). This turns out to also give good agreement with the experimental results for nickel (Burhop 1940; Smick & Kirkpatrick 1945). More detailed analysis of the cross sections are available, but these generally involve the evaluation of complicated multiple integrals (Burhop 1940; Arthurs & Moisewitsch 1958). Considering the number of uncertainties in the astrophysical model, this simplified cross section (equation [8]) should be sufficiently accurate for the other elements within the supernova envelope.

The equation (5) for the energy loss contains a logarithmic term that changes sign when the electron kinetic energy becomes less than the mean excitation per collision, which we take to be a constant. For elements such as iron and nickel, this happens at approximately 300 eV. Below that energy this loss term formally changes sign, as if the electron were to increase in energy as it travels through the medium. This problem is only apparent, however. It neglects the fact that I_{avg} must decrease as T becomes small, always being less than T from energy conservation. For this reason, the energy loss equation with constant I breaks down at energies below 300 eV (ICRU Report 37). To avoid this problem, we adopt the solution from the ICRU Report of using a cutoff energy for the integral, in this case 1 keV. Below this value, the differential range is assumed to be linearly proportional to the electron energy as it decreases to zero. This enables the range to be computed in two parts. The first part used equation (5) to compute the range $R(T_i \rightarrow T_c)$ from the incident electron energy down to the cutoff energy T_c. For the second part, from T_c down to zero, the differential range is assumed to be proportional to the electron kinetic energy. Therefore the electron range is calculated by

$$R(T_i \rightarrow 0) = R(T_i \rightarrow T_c) + \frac{1}{(dE/dx)_c}\int_{T_c}^{0} \frac{T}{T_c}\, dT, \quad (9)$$

and $(dE/dx)_c$ is value of the energy loss at the cutoff energy T_c. In the case of the chosen cutoff of 1 keV, the range is, however, dominated by the first term. For pure iron, this correction amounts to only 0.2% of the total range for a 10 keV electron and gets smaller as the electron energy increases. This small correction is included for the purposes of comparing the range results with those computed in the ICRU Report (1984).

We assume that the electrons decelerate in a medium of constant density; that is, that they decelerate in a time much shorter than the remnant age and that they have insufficient range to cross from one supernova zone to the next (CT). We also assume that the K electrons liberated by electron impact contribute to the heating and to outer-shell ionization but are of sufficiently low energy ($\sim I_{avg}$) that they do not contribute significantly to the creation of additional K-shell vacancies, at least not for heavy elements. The energy loss equation (5) is dominated by ionization of outer-shell electrons. Each electron T_i produces about T_i/I_{avg} primary collisional ionizations with energies in the hundreds of eV range. These primary electrons in turn cause secondary ionization of (necessarily) lower energy. The total ionization rate can be calculated in this way (Swartz 1991), but with an eye toward X-ray astronomy we will concentrate on the K vacancies.

Elements with atomic numbers above hydrogen have two electrons in the K shell. After one electron is ejected, the cross section changes for ejection of the second electron. We assume here that the probability of the second electron being ejected before the K vacancy is filled is small enough to be ignored. Few ions with a K vacancy exist as targets for a second ionization because the lifetime of the electron hole in the K shell is only of order 10^{-14} s (Bambyneck et al. 1972).

3. RESULTS

In Figures 1–5 we show as solid lines the radial distribution of the total electron power per gram. Dashed, dotted, and dot-dashed curves represent contributions of photoelectrons, Compton electrons, and positron kinetic energy to that total energy deposition rate, showing their distributions in the supernovae ejecta for models of Type II (SN11E1 model for SN 1987A), Type Ia (model W7) and its fully mixed counterpart, and Type Ib (model WR6C) and its fully mixed counterpart, each at several different times. The same figure for SN 1987A model W10hmm has been presented by The et al. (1990). For all models we see from these figures that the electron power from Compton scattering is at least a factor of 10 larger than that from the photoelectrons, and that this ratio becomes even larger for the outer envelope since there are less heavy elements than in the core; however, both rates decrease with increasing enclosed mass. Compton scattering is the dominant energy deposition mechanism in a scattering-dominated medium. However, where the envelope is thin, near the envelope surface where most of gamma lines escape directly at late times, the positron kinetic energy provides the dominant source of energy deposition. The flatness of the positron kinetic energy deposition in Figures 3 and 5 for fully mixed models occurs because the fraction of ^{56}Co is constant everywhere and, accordingly, so too is the amount of positron power per gram. The reader should note that the positron kinetic energy deposition presented here is calculated by assuming the positron to lose its kinetic energy instantly after being produced in the decay of ^{56}Co. This is an overestimate, as the positron does not stop instantly after being produced and may even escape from the ejecta as it thins (see Fig. 3 of CT). However, our calculations confirm that at late times in a transparent gamma-ray envelope, the positron kinetic energy deposition provides the dominant process of energy deposition, especially for mixed models, as has been shown by Arnett (1979).

We show how each mechanism of energy deposition evolves with time in Figures 6–10, each for a different type of supernova. They display the fractions of energy deposited in the entire supernovae ejecta by Compton scattering (f_{scat}), photoelectric absorption (f_{pe}), positron kinetic energy (f_{kin}) from ^{56}Co β^+ decay, as well as the fraction of total energy ($1 - f_{\gamma+X}$) that does not escape, where f_γ and f_X are, respectively, the fractions of the total radioactive power that emerge as gamma lines

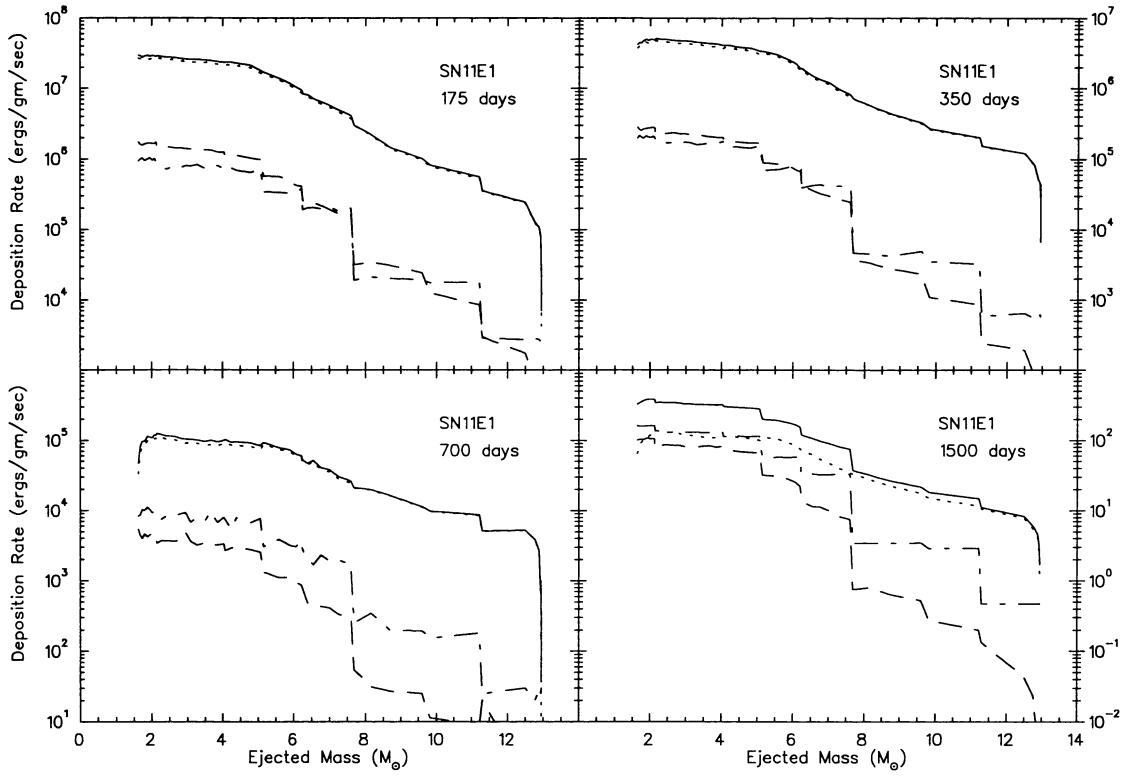

FIG. 1.—Energy deposition rate (ergs/g/s) as function of enclosed mass for model SN11E1 at days 175, 350, 700, and 1500. Long-dashed lines, dotted-lines, and long dashed-dotted lines show the energy transfer to the gas by mechanism: photoelectric absorption, Compton scattering by photons, and positron kinetic energy transfer respectively. The solid line shows the total of all these processes. The figures show that in almost all cases, Compton scattering is the dominant process.

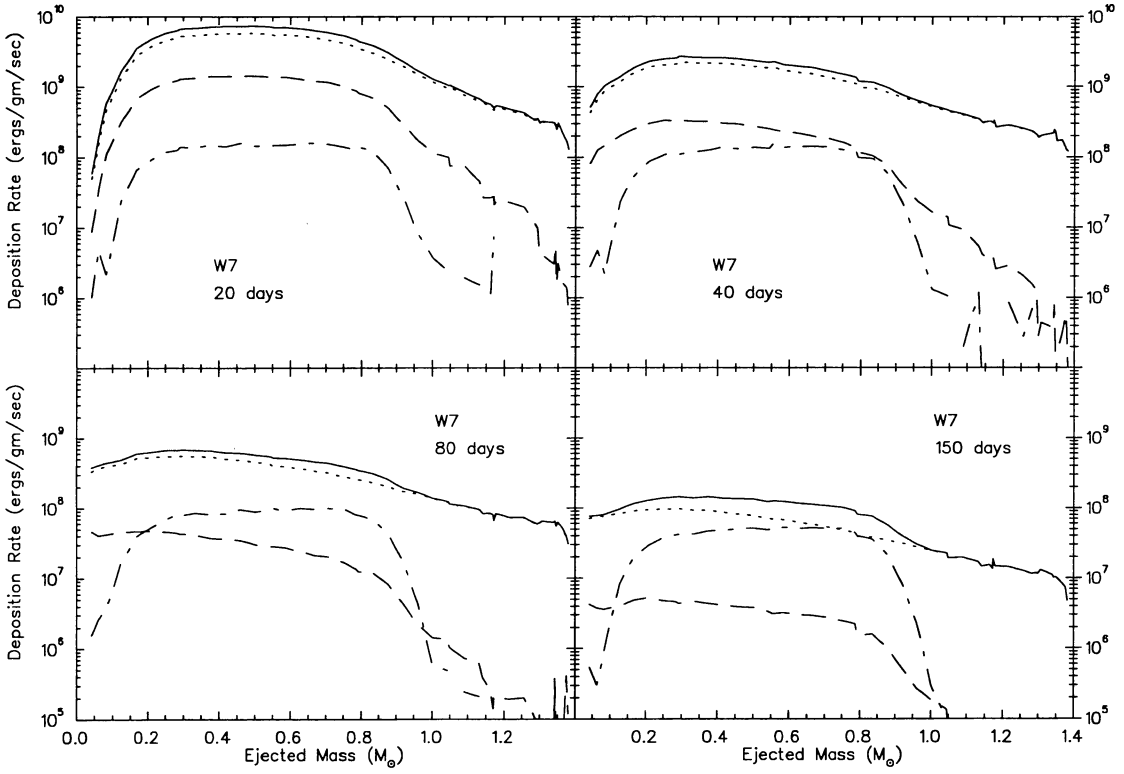

FIG. 2.—Same as Fig. 1, but for model W7 at days 20, 40, 80, and 200

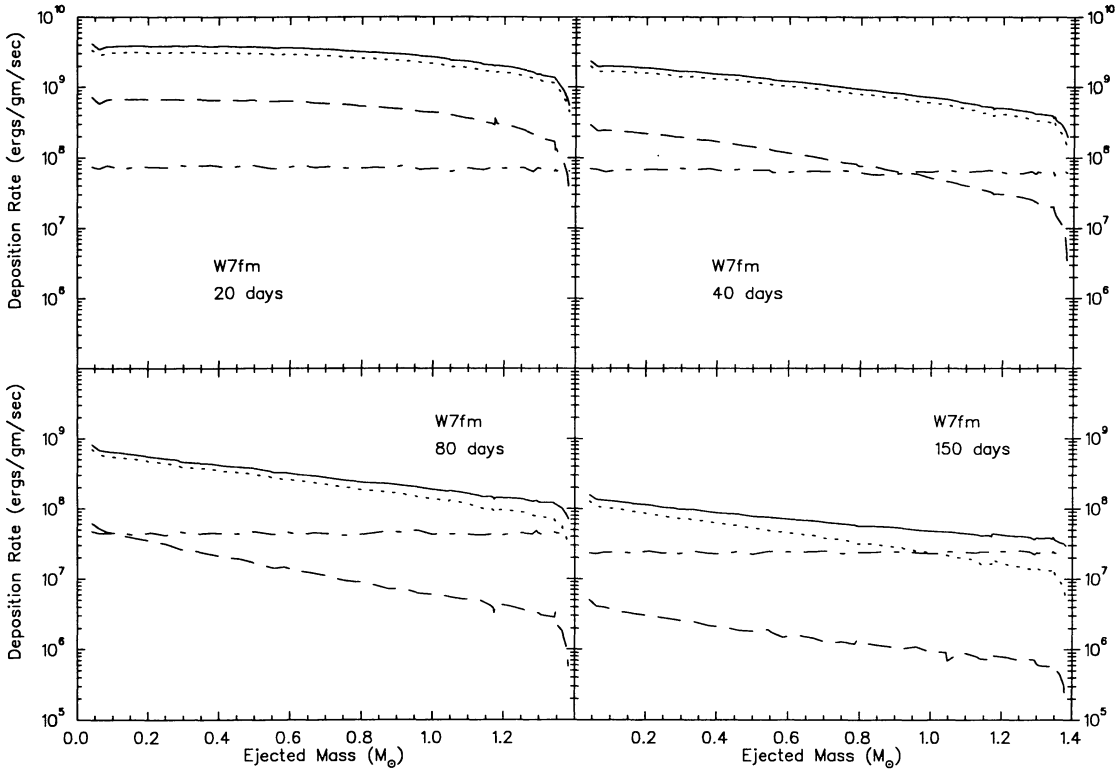

FIG. 3.—Same as Fig. 1, but for model W7fm at days 20, 40, 80, and 200

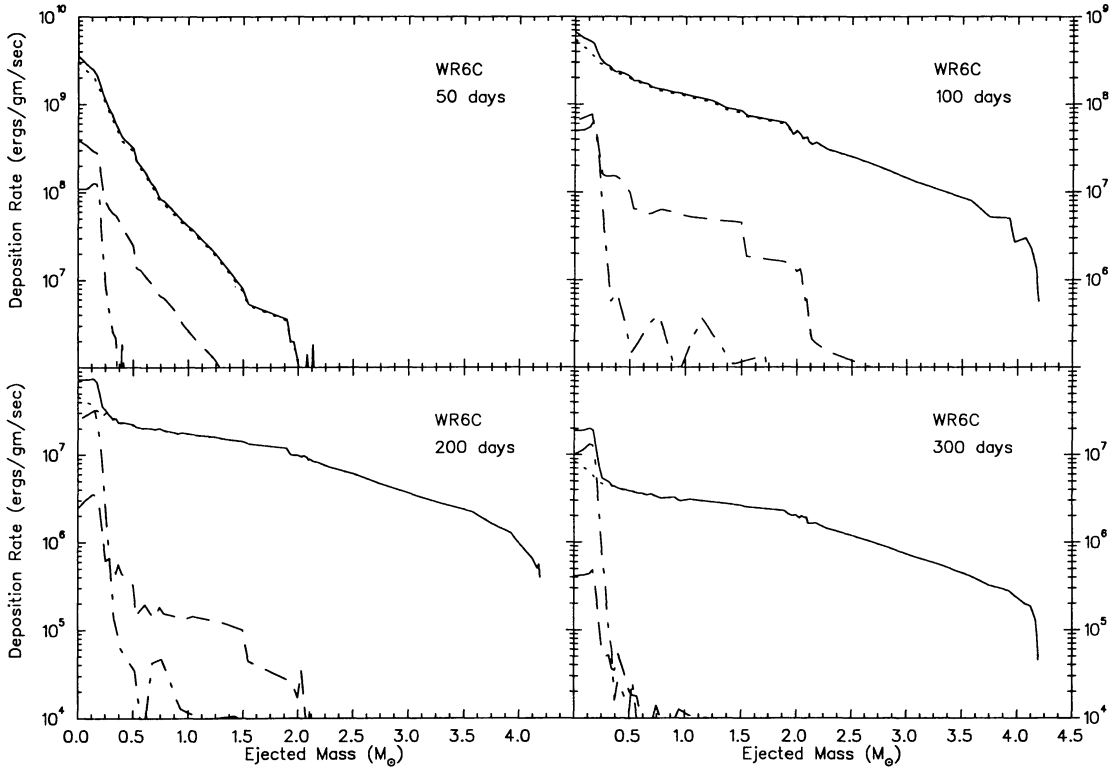

FIG. 4.—Same as Fig. 1, but for model WR6C at days 50, 100, 200, and 300

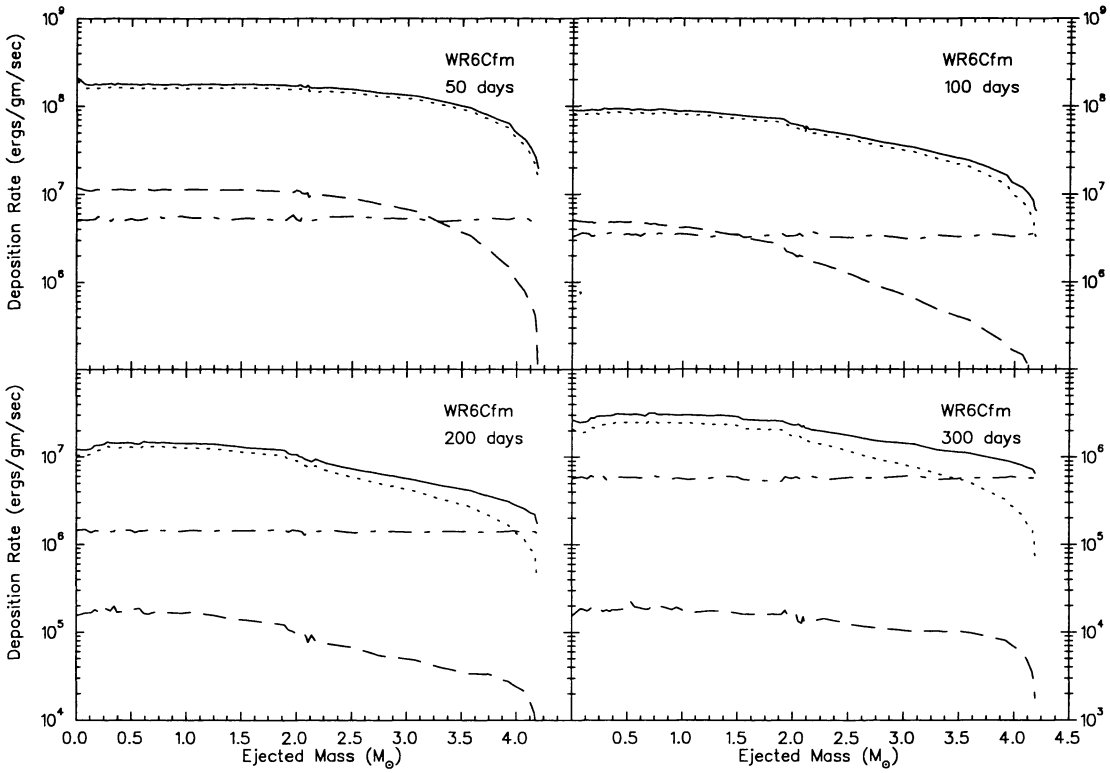

FIG. 5.—Same as Fig. 1, but for model WR6Cfm at days 50, 100, 200, and 300

and as Compton continuum. The photoelectric and Compton scattering energy depositions decrease monotonically with time, with f_{pe} dropping slightly faster than f_{scat} (except for late times in SN 1987A models when low-energy gammas from ^{57}Co increase f_{pe}). The quantity f_{kin} is a constant for all times when ^{56}Co is the power source. Again at late times f_{kin} is larger than f_{scat} because most gamma rays at these times escape directly rather than being scattered. Our results below for K-shell vacancy rates are compromised for times when $f_{kin} > f_{scat}$ because our computation does not record the positron energy spectrum and therefore does not calculate the K-vacancy rate due to positron collisions during their deceleration. Were this shortcoming easy to correct we would have done so; however, the fate of positrons in the thin expanding envelope is complicated by other difficulties regarding the true physical nature of the ejecta. Nevertheless we include the deposition energy of gamma rays created in positron annihilations in our gamma-ray transport, assuming the positrons to annihilate instantaneously. Much work remains to be done on the late spectrum of Type I's, as these comments indicate.

For supernova light curve and spectra calculations, an accu-

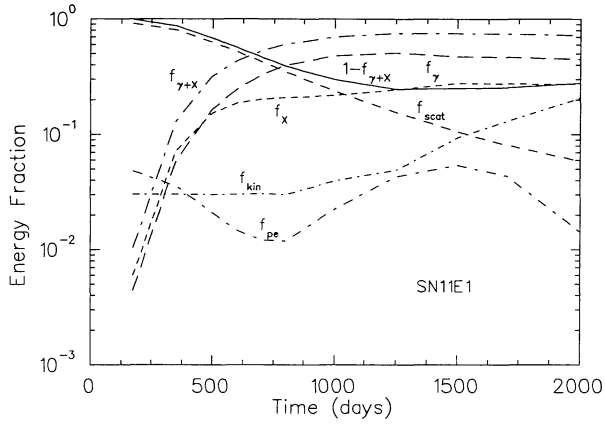

FIG. 6.—Time evolution of fraction of energy from the radioactive decays that ends up distributed as escaping X-rays (f_X) or gamma rays (f_γ); or distributed to the matter in the envelope via photoelectric effect (f_{pe}), Compton scattering (f_{scat}), or positron kinetic energy (f_{kin}) for model SN11E1. The quantity $f_{X+\gamma}$ is the fraction of energy escaping as X- or gamma-radiation. The solid line represents the quantity 1-$f_{X+\gamma}$ which is the fraction of energy that goes into heating the envelope.

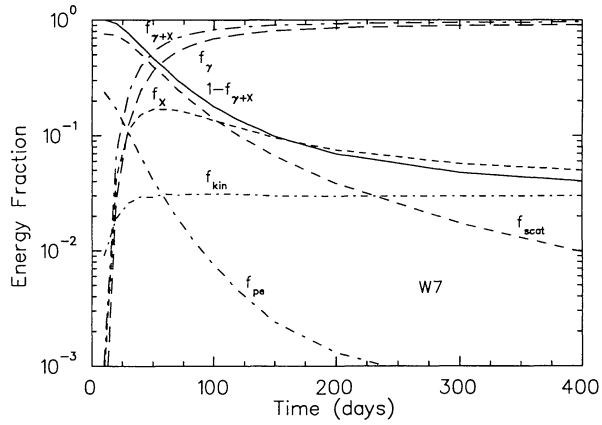

FIG. 7.—Same as Fig. 6, but for model W7

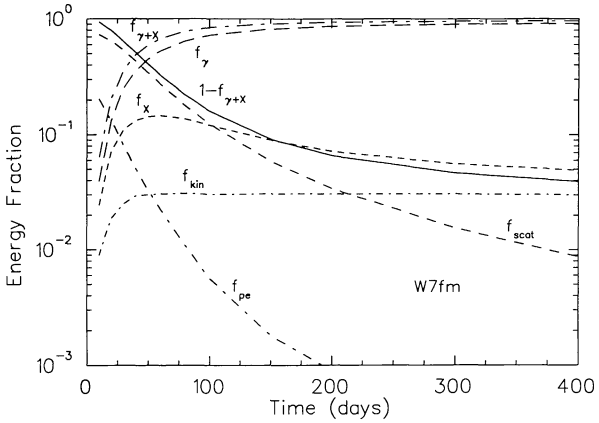

FIG. 8.—Same as Fig. 6, but for model W7fm

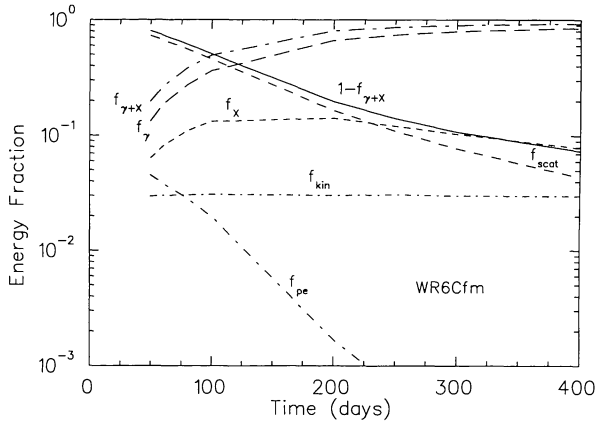

FIG. 10.—Same as Fig. 6, but for model WR6Cfm

rate deposition energy into the supernova ejecta is essential. In many calculations the deposition energy has been assumed to follow an approximate formula; here we present in Table 1 the result of a fitting function $f_{dep} = 1 - \exp(a + b/t^2 + c/t^4 + d/t^6)$ to the calculated f_{dep} of supernova models considered here. We write f_{dep} as a function of $1/t^2$ because f_{dep} decreases with decreasing γ-ray optical depth τ_γ and $\tau_\gamma \propto 1/t^2$. The last column in Table 1 shows the largest percentage difference between each calculated f_{dep} and fitted f_{dep}. The f_{dep} fit of model W7 and WR6C and their fully mixed counterparts shown in Table 1 are obtained by fitting f_{dep} up to day 400. The f_{dep} for model SN11E1 and W10hmm are fitted up to day 2000, and the late times produce the largest deviation from the model's f_{dep} because near day 1000, the energy source from ^{57}Co starts to dominate the light curve, and this changes the shape of f_{dep} curves.

Figures 6–10 also show the fractions of total radioactive power that escape as gamma lines (f_γ), as X-ray continuum (f_X), and their sum ($f_{\gamma+X}$). At early times, f_X is larger than f_γ because the ejecta is still thick enough that most gamma rays are scattered before escaping. However after about 500 days for W10hmm and SN11E1 of Type II, the fraction escaping as gamma lines becomes larger than the fraction escaping as X-ray continuum. For the unmixed model W7 of Type Ia that crossover happens at 30 days, and it occurs earlier than 10 days

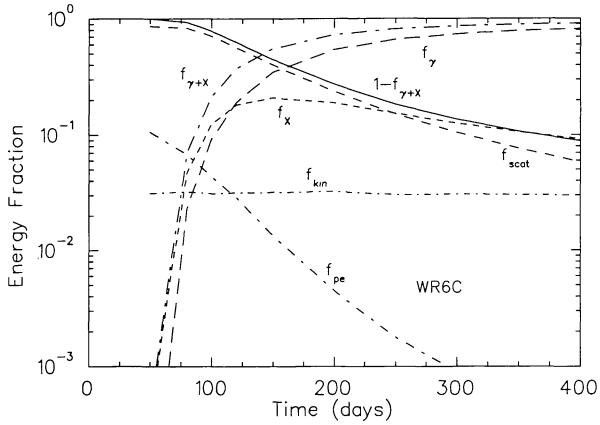

FIG. 9.—Same as Fig. 6, but for model WR6C

for fully mixed model W7fm of Type I (not visible on Fig. 8), at 125 days for model WR6C of Type Ib, and earlier than 50 days for fully mixed model WR6Cfm of Type Ib. The mixed models have larger escape fractions at early times than do their unmixed counterparts because the mixing put much of the radioactive source at lower optical depth. A mixed model therefore has lower fraction of energy deposited ($f_{dep} = 1 - f_{\gamma+X}$) than an unmixed model. For W7 and W7fm the difference in f_{dep} is about 12% at day 80 and the difference between WR6C and WR6Cfm is about 35% at day 100.

Although Compton scattering is the dominant energy deposition mechanism, the ratios of energy deposition rates vary among different elements in the ejecta. In Figure 11 we show for several elements the K-shell vacancy rate per gram for W10hmm as a function of mass. The separate K ionization processes are shown in separate panels, except that for Fe the vacancy rate from ^{56}Co electron captures is shown as a dotted line in the photoelectric panel, where it is comparable to the Fe photoelectric rate (dashed line) from the Compton continuum. For the other elements (Si, O, He) shown, no e^--capture source exists, so the four panels display, respectively, their K ionization rates due to photoelectric gamma continuum, Compton scattering, bremsstrahlung photons, and collisions with Compton electrons. The element format is in panel b, and is identical in Figures 11–16. It is clear from these figures that photoelectric absorption is (except for ^{56}Co e^--capture) the main cause of K-shell ionization of iron (solid lines), being larger by two orders of magnitude than other processes for that element. The K-shell ionization of iron by inelastic electron scattering is so small that even bremsstrahlung and Compton scattering create comparable vacancy rates. The result for SN11E1 model shown in Figure 12 is similar to that of W10hmm, not surprisingly since both of them are models of Type II supernova SN 1987A. At any time and any model, we see that ^{56}Co electron-capture and K-shell ionization of iron by photoelectric absorption from the Compton continuum are the dominant processes for that element. Their competition depends strongly on the degree of mixing, most dramatically comparing panel (*a*) for WR6C with panel (*a*) for WR6Cfm. In the first case no ^{56}Co exists outside of 0.5 $M_\odot$ in the ejecta, so it cannot contribute there. We notice that the statistics of Compton scattering K-vacancy rate curves for Fe are not as good

TABLE 1

FITTING PARAMETERS OF f_{dep}

	$f_{dep} = 1 - \exp(a + b/t^2 + c/t^4 + d/t^6)$, with t in days				
MODEL	a	b	c	d	Percent Max Different
W10hmm	-2.09×10^{-1}	-2.15×10^{5}	$+1.84 \times 10^{9}$	-3.43×10^{12}	13
SN11E1	-2.67×10^{-1}	-1.31×10^{5}	-1.60×10^{10}	$+4.91 \times 10^{14}$	13
W7	-3.11×10^{-2}	-1.65×10^{3}	$+3.06 \times 10^{5}$	-2.10×10^{7}	3
W7fm	-3.28×10^{-2}	-1.37×10^{3}	$+3.76 \times 10^{5}$	-2.66×10^{7}	6
WR6C	-1.32×10^{-2}	-1.21×10^{4}	-2.51×10^{7}	...	4
WR6Cfm	-3.15×10^{-2}	-7.46×10^{3}	$+9.03 \times 10^{6}$	...	3

(jagged structure) as for the photoelectric absorption, but since the photoelectric K-vacancy rate is much larger than that from the scattering, this inaccuracy is dwarfed by the dominant and smoother photoelectric K-vacancy rate curve. For lighter elements, the situation differs, a point that we return to below.

We note for the reader that the rates in Figure 11 can easily be converted into lifetimes for K-shell ionization. In Figure 11, for model W10hmm, for example, at day 350 the photoelectric rate 1.3×10^{11} g^{-1} s^{-1} near $m = 6\ M_\odot$ corresponds to an Fe lifetime against photoelectric absorption of Comptonized gammas equal to 3.8×10^{8} s. This conversion requires noting only that at that coordinate in W10hmm the mass fraction X(Fe) = 0.0046, or 5.0×10^{19} Fe/g. The composition of W10hmm can be found in Figure 1 of Pinto & Woosley (1988b). This roughly 13 yr lifetime of Fe against K-shell ionization is much longer than the age of the remnant, illustrating that most Fe atoms will not suffer this fate during the subsequent expansion. At earlier times the lifetime was much shorter owing to the much higher flux. Similarly, lifetimes for each process and for each element can be calculated; we show in Table 2 the lifetimes of Fe against each process of K-shell ionization at several radius mass coordinates $m(r)$. The iron mass fraction X_{Fe} is also listed; but the Fe lifetime is, for small X_{Fe}, independent of its value. For lighter elements, refer to the figures.

Figures 13–16 show the K-shell vacancy rates per gram for Type Ia and Type Ib models. Both W7 and WR6C show near the center, where Fe dominates the composition, that all four

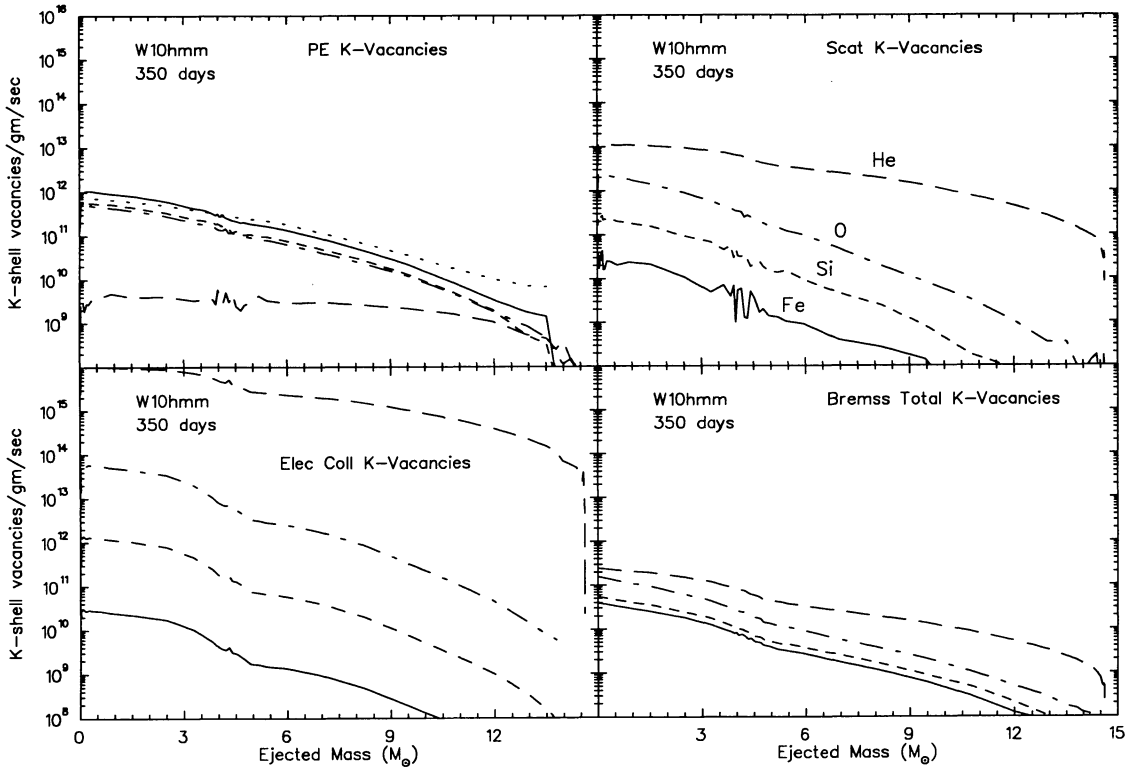

FIG. 11.—K-vacancy rate per g per s as function of enclosed mass for W10hmm. The figure shows the K-vacancy generation rate for model W10hmm for ages of 350 days. The four panels in the figure illustrate the K-vacancy generation rate by the four major mechanisms: (*a*) photoelectric effect, (*b*) Compton scattering, (*c*) electron collision, and (*d*) bremsstrahlung photons. Long-dashed lines, long dashed-dotted lines, short-dashed lines, and solid lines represent the K-vacancy rates for He, O, Si, and Fe, respectively. Dotted line represents the ^{56}Fe K-vacancy rates created directly by electron captures by the ^{56}Co nucleus.

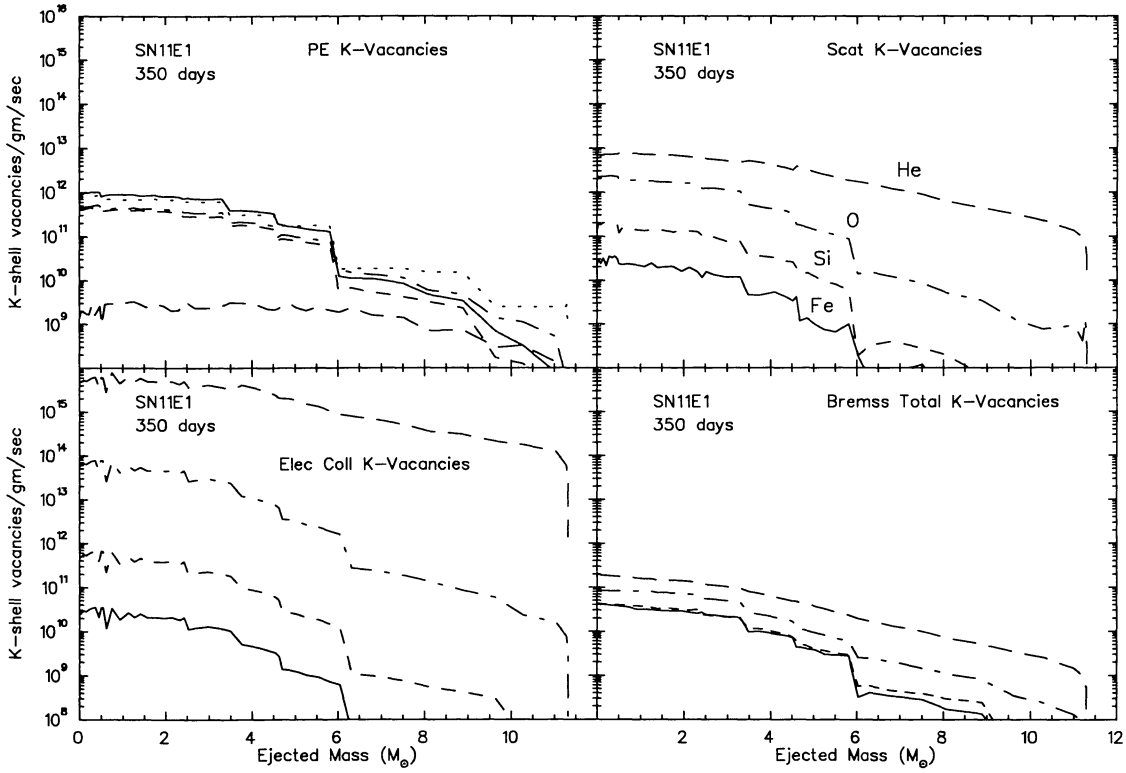

FIG. 12.—Same as Fig. 11, but for model SN11E1 at 350 days

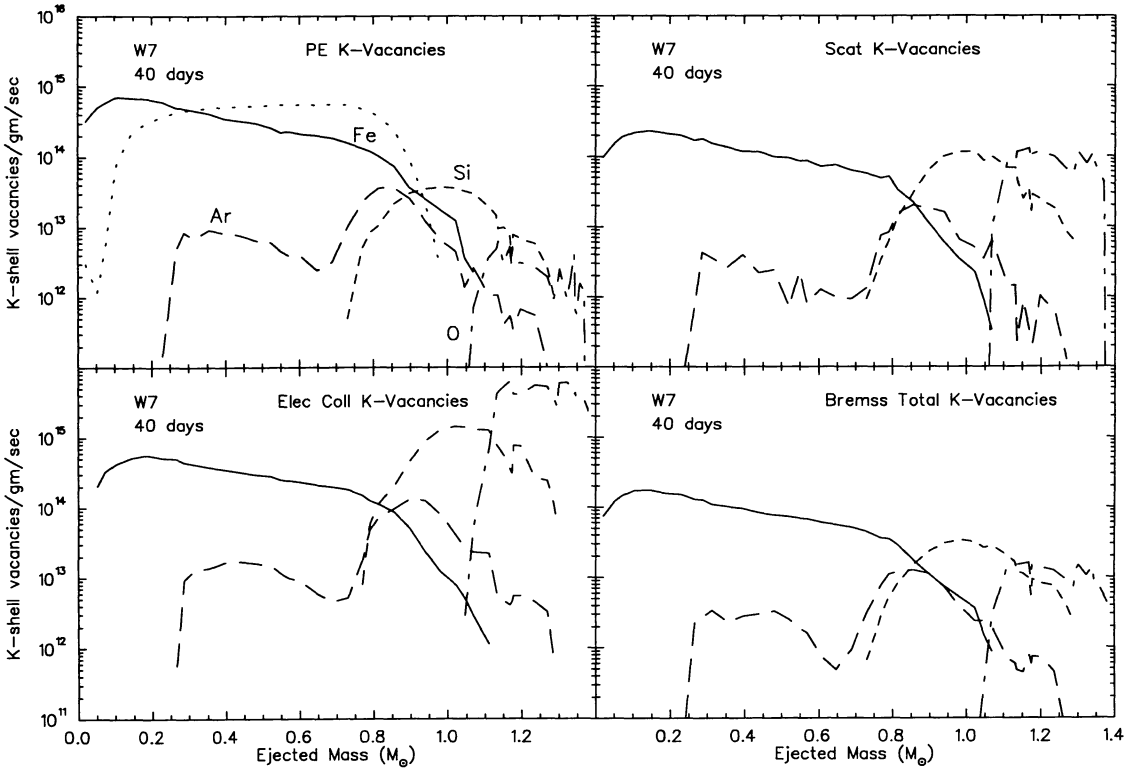

FIG. 13.—Same as Fig. 11, but for model W7 at 40 days

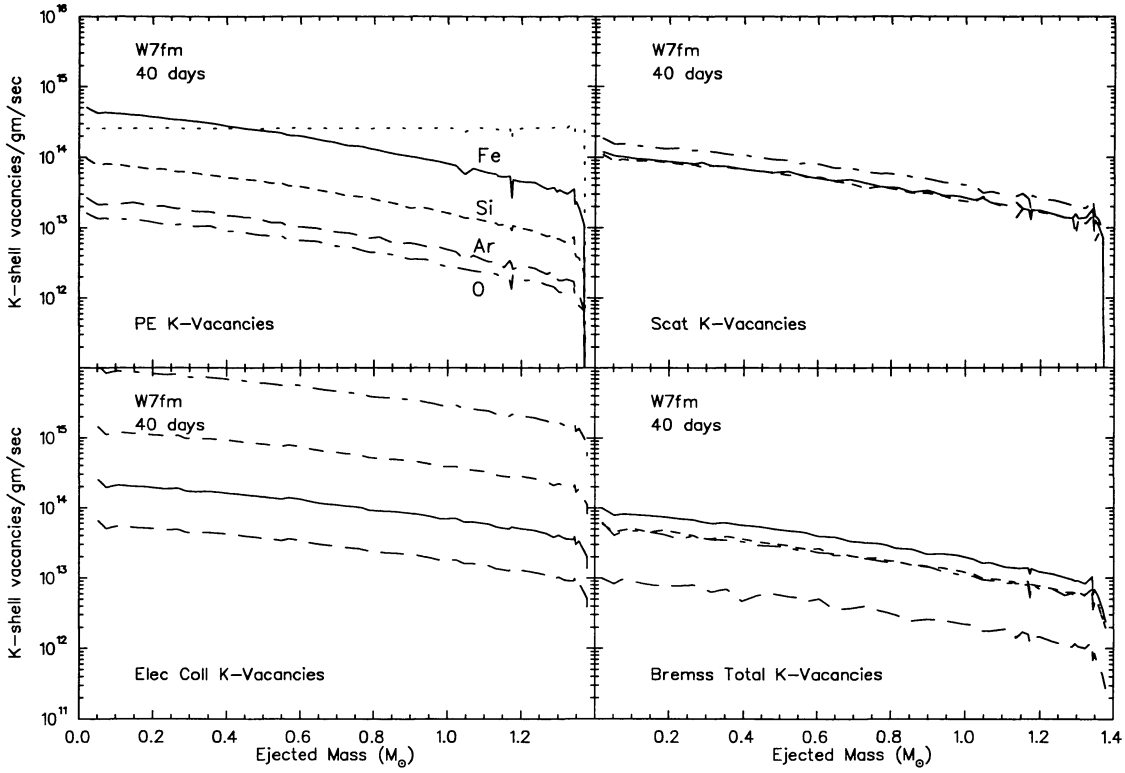

FIG. 14.—Same as Fig. 11, but for model W7fm at 40 days

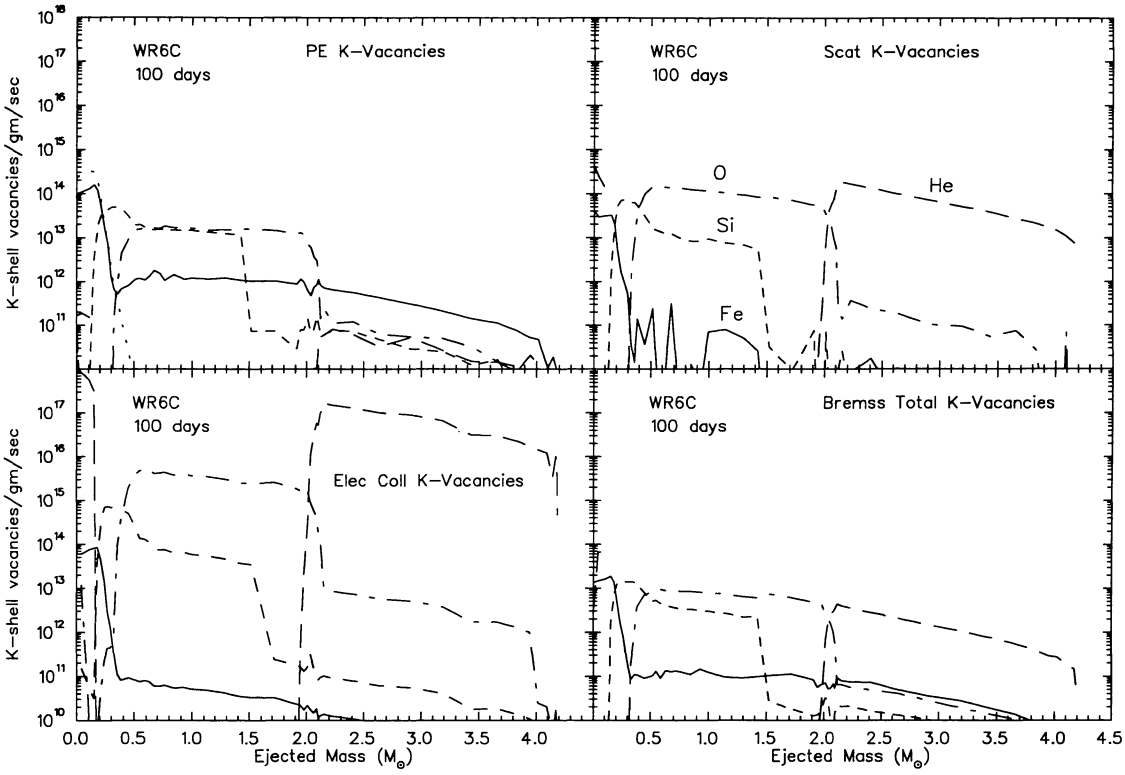

FIG. 15.—Same as Fig. 11, but for model WR6C at 100 days

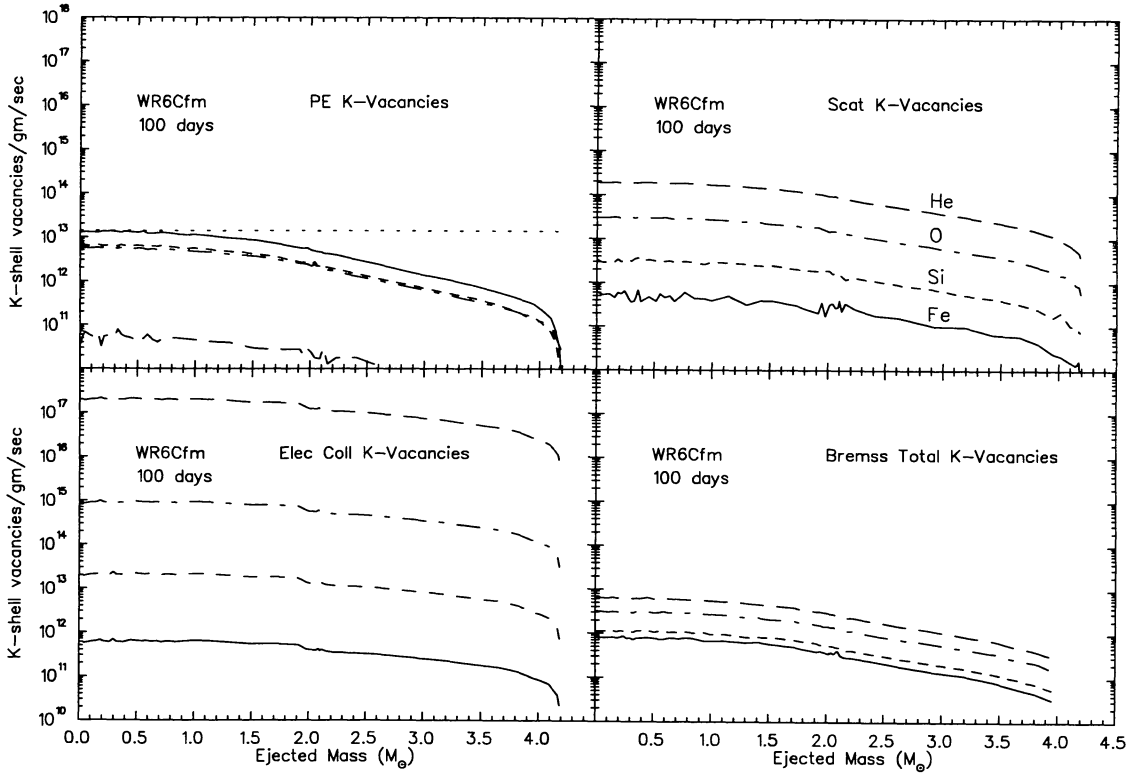

FIG. 16.—Same as Fig. 11, but for model WR6Cfm at 100 days

processes of K-shell ionization of Fe are comparable; however, farther out, where intermediate elements dominate the composition, the Fe photoelectric absorption of Comptonized gammas dominates K-vacancy rates for Fe, just as it does for the mixed models of SN 1987A. And for fully mixed W7fm all four processes are important throughout. For model WR6C, at the outer envelope beyond $m = 2\ M_\odot$ where He is the dominant constituent, the ratio between the K-shell vacancy rate of Fe due to photoelectric absorption and that due to electron collision is even larger than in the inner envelope of intermediate-mass elements. These examples along with Table 2 show that the local composition influences the relative K-shell vacancy rates of Fe.

The K-shell photoelectric ionization by Comptonized gammas becomes less important for lighter elements because they have smaller photoelectric cross sections in the 10–30 keV energy range where most absorption of the abundant Comptonized gammas occurs. For light elements such as ^{4}He or ^{16}O, photoelectric absorption of the bremsstrahlung photons, which are abundant at lower energies (CT), creates more K-

TABLE 2

Fe LIFETIMES AGAINST K-SHELL IONIZATION PROCESSES IN MODEL W10HMM

m_r ($M_\odot$)	X_{Fe}	Age (days)	PE (s)	Compton (s)	e^- Collision (s)	Bremsstrahlung (s)
1	1.64×10^{-2}	175	4.2×10^{7}	1.7×10^{9}	1.6×10^{9}	1.5×10^{9}
		350	2.0×10^{8}	8.2×10^{9}	7.2×10^{9}	6.1×10^{9}
		700	8.8×10^{9}	3.0×10^{11}	2.3×10^{11}	2.2×10^{11}
4	7.86×10^{-3}	175	4.5×10^{7}	2.2×10^{9}	4.4×10^{9}	2.2×10^{10}
		350	2.5×10^{8}	3.2×10^{10}	2.0×10^{10}	1.1×10^{10}
		700	1.3×10^{10}	1.0×10^{12}	7.6×10^{11}	5.1×10^{11}
8	2.96×10^{-3}	175	6.8×10^{7}	7.6×10^{10}	1.2×10^{10}	7.1×10^{8}
		350	6.2×10^{8}	1.3×10^{11}	5.9×10^{10}	2.7×10^{10}
		700	4.1×10^{10}	8.3×10^{12}	2.6×10^{12}	2.0×10^{12}
12	2.48×10^{-4}	175	4.6×10^{7}	3.2×10^{11}	3.3×10^{10}	2.9×10^{9}
		350	1.4×10^{9}	1.9×10^{13}	9.3×10^{10}	2.2×10^{10}
		700	5.3×10^{10}	1.9×10^{15}	2.7×10^{12}	1.7×10^{12}

shell vacancies than does the photoelectric absorption of the Comptonized gammas. The lighter the atom, the larger are the ratios of K-shell ionization rates due to inelastic electron scattering, Compton scattering, and bremsstrahlung relative to that due to photoelectric K-shell ionization. For Si in Type II SNs, the K-shell ionization due to electron collisions start to compete with the K-shell ionization due to photoelectric. This is even more noticeable in Type I, electron collisions create more Si K-shell vacancies than other processes (see Fig. 13), with Compton scattering and photoelectric absorption being comparable to each other but larger than that due to bremsstrahlung. For O the situation begins to differ in that electron collisions result in more O K-shell ionizations than that of other processes, at least 10 times more for Type Ib and Type II or 100 times more for Type Ia. The photoelectric absorption rate of O in any type of supernovae is clearly less than the Compton scattering ionization rate, and, in fact, the photoelectric absorption rate for O is so small that it is comparable with the bremsstrahlung ionization rate. These trends are easily understandable in retrospect in terms of the rates of the fundamental processes. But we believe that our very detailed numerical models will assist the discerning reader's evaluation of them.

We also find that the K-shell vacancy rates of elements lighter than Fe are not significantly enhanced by the K X-rays from Fe. At early times the Fe K X-ray rate is due to photoelectric, Compton scattering, and electron capture Fe K-vacancies. But at later times as the fraction of escaping gamma lines becomes higher, most Fe K-vacancies are due to electron capture branch of ^{56}Co → ^{56}Fe decays. However, the 6.4 keV Fe K X-ray mostly are photoabsorbed by Fe K-shell electrons which then emit Fe L X-ray with much lower intensities since the Fe L-shell radiation yield is $\sim 3.8 \times 10^{-4}$. Therefore the total K-vacancy rate of elements lighter than Fe caused by Fe K X-ray electron capture is $\sim 9.6 \times 10^{-5}$ ^{56}Fe decay rate. This certainly much smaller than K-vacancy rate shown in Figures 13–16. It is interesting that at very late times when $f_{\rm scat} < 4 \times 10^{-4}$), Fe K X-ray from electron capture will become the cause of the dominant energy deposition to electrons in the ejecta.

For the very light elements such as He, the electron collisions create at least 100 times more K-shell ionization for Type II and between 100 and 1000 times more for Type Ib than the next closest ionizing process, which is Compton scattering. The bremsstrahlung He K-vacancy rate is larger than that of photoelectric absorption of Comptonized gammas. CT had predicted that for light elements the bremsstrahlung ionization rates would exceed those from gammas owing to the ω^{-3} cross section.

In order to examine the time evolution of K-shell vacancies of each element, we show in Figure 17 the rate of K-shell vacancies per gram of ejecta mass for He, O, Si, Fe versus time for two different mass coordinates. For this comparison the e^--capture by ^{56}Co is not included in the Fe total rate. We find for this model W10hmm of SN 1987A that the K-shell vacancy rates of all elements are monotonically decreasing. This result does not support Graham's (1988) interpretation that the increase in the feature of He I 1.083 μm in the infrared spectrum of SN 1987A (Elias et al. 1988) is due to the increase of He ionization in the outer layer owing to more radiation escaping from the core between day 76 and day 135. Our demonstration

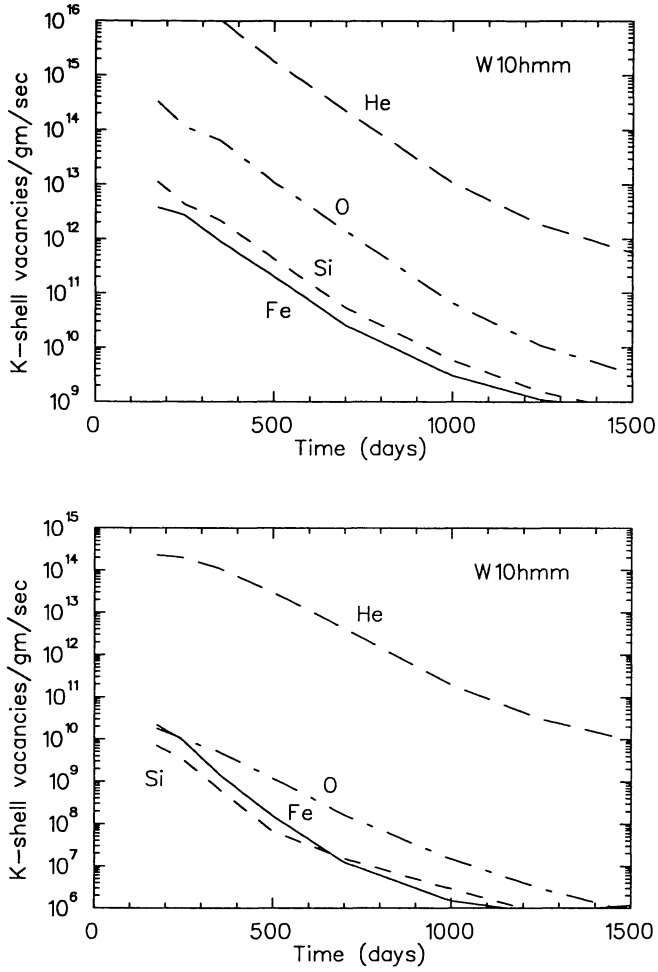

FIG. 17.—Time evolution of K-shell vacancy rates of model W10hmm. Long-dashed lines, long dashed-dotted lines, short-dashed lines, and solid lines represent the K-vacancy rate per gram at mass coordinate $m(r) = 0.034\ M_\odot$ (*top*) and $m(r) = 13.7\ M_\odot$ (*bottom*) of He, O, Si, and Fe, respectively. The Fe K-vacancy rates shown as solid lines do not include the ^{56}Fe K-vacancy rates created directly by electron captures by the ^{56}Co nucleus.

is for a progressively mixed model, as SN 1987A appears to have been; but for a central radioactivity model (not studied here), the He ionization will indeed increase when the diffusion of gammas reaches the photosphere. Figure 18 shows the evolution of the K-shell vacancy rates for the same elements in a Type Ia model.

In Tables 3–7 we tabulate some of the strongest K X-ray fluxes at Earth for all models (for K X-rays of lower energy, a more accurate calculation of the transport of lower-energy photons and finer zone distribution in the models is needed). This calculation differs fundamentally from those for the vacancy rates discussed above, because it depends upon the fraction of the X-rays that actually escape the supernova structure. In all supernova models considered here, the Fe K X-ray flux is at least two orders of magnitude stronger than any other K X-ray lines, although K-shell vacancy rates of lighter elements can be as much as three orders of magnitude larger than that of Fe. For each K X-ray flux we also tabulate (in percent) the fraction of the escaping photons that had been created by pri-

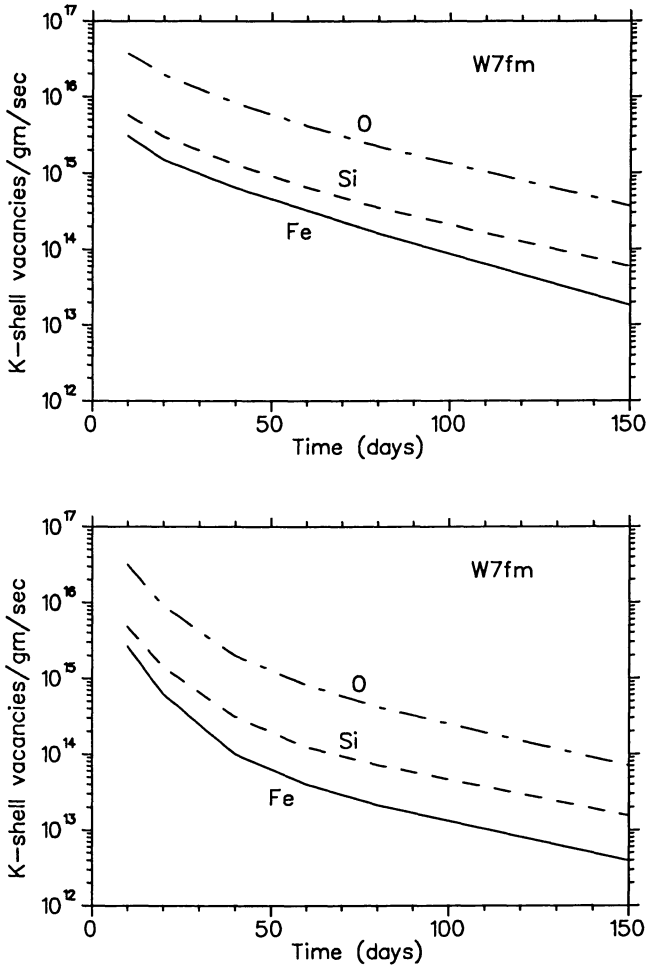

FIG. 18.—Same as Fig. 17, but for model W7fm at mass coordinate $m(r) = 0.21\ M_\odot$ (*top*) and $m(r) = 1.21\ M_\odot$ (*bottom*).

mary photons (photoelectric and Compton scattering), electron collisions, and bremsstrahlung processes. The relative production fractions of these photons that actually escaped the supernova model are not the same as the relative bulk production throughout the model. The lower the X-ray energy, the closer its emission must be to the surface if it is to escape. CT made this point explicitly for bremsstrahlung. In Type II supernova, for elements heavier than Si the largest contribution to the K X-ray flux comes from the photoelectric process, and for lighter elements the largest contribution to the K X-ray flux comes from electron collision process. However, the relative contributions from electron collision and bremsstrahlung increase with time, although they never overtake the photoelectric absorption contribution in type II. In Type I supernova, the contribution of photoelectric absorption to K X-ray flux is larger at early times than the other two processes. However, electron collision and bremsstrahlung contributions grow with time so that at later times they are comparable with photoelectric absorption contribution. At even later times electron collision can be the dominant contributor to K X-ray flux.

4. DISCUSSIONS AND CONCLUSIONS

Our Monte Carlo calculations of the energy deposition in explicit numerical supernova models follow explicitly the energy transfer from gamma rays to excitation of inner-shell electrons. The energy input is the gamma rays from radioactive decay of ^{56}Co, which deposit their energy by Compton scattering and photoelectric absorption. In addition to that, positrons from ^{56}Co decays deposit their kinetic energy into the envelope. Energy deposition fraction $(1 - f_{\gamma+X})$ curves in Figures 6–10 are also of special interest to investigators studying supernova light curves (Arnett 1979, 1989, 1982; Colgate, Petscheck, & Kriese 1980; Chevalier 1976, 1981; Sutherland & Wheeler 1984; Weaver, Axelrod, & Woosley 1980). They show the rate of energy deposition as function of time and mass radius of each supernova model. Compton scattering is by far the most dominant energy deposition at early times. At very early times the photoelectric energy deposition is also larger than the positron kinetic energy deposition, but later the positron kinetic energy deposition becomes greater, especially near the surface of the envelope. After around day 1500 for Type II, around day 250 for Type Ia, and around day 600 for Type Ib, the positron kinetic energy deposition starts to take over. At last, it becomes the dominant energy deposition mechanism (Arnett 1979).

TABLE 3

MODEL W10HMM K X-RAY FLUXES

TIME (days)	Si ($cm^{-2}\ s^{-1}$)[a]			S ($cm^{-2}\ s^{-1}$)[a]			Ar ($cm^{-2}\ s^{-1}$)[a]			Fe ($cm^{-2}\ s^{-1}$)[a]			
	Photon	Coll.	Brems.	Photon	Coll.	Brems.	Photon	Coll.	Brems.	e^--Capture	Photon	Coll.	Brems.
175		5×10^{-9}			8×10^{-9}			6×10^{-9}			5.5×10^{-6}		
	90	0	10	94	0	6	91	0	9	48	51	0	1
350		1×10^{-9}			7×10^{-9}			7×10^{-9}			9.3×10^{-6}		
	66	8	26	82	2	16	89	1	10	70	29	0	1
700		4×10^{-10}			2×10^{-9}			1×10^{-9}			2.0×10^{-6}		
	77	13	11	84	9	7	89	5	6	87	13	0	0
1500		7×10^{-11}			4×10^{-10}			2×10^{-10}			7.4×10^{-8}		
	97	2	0	99	1	0	100	0	0	0	100	0	0

[a] Assuming distance of 50 kpc and no interstellar absorption.

TABLE 4

MODEL SN11E1 K X-RAY FLUXES

TIME (days)	Si (cm^{-2} s^{-1})[a]			S (cm^{-2} s^{-1})[a]			Ar (cm^{-2} s^{-1})[a]			Fe (cm^{-2} s^{-1})[a]			
	Photon	Coll.	Brems.	Photon	Coll.	Brems.	Photon	Coll.	Brems.	e^--Capture	Photon	Coll.	Brems.
175		5×10^{-10}			1×10^{-9}			5×10^{-9}			7.0×10^{-6}		
	85	11	5	87	3	10	97	0	2	84	16	0	0
350		6×10^{-10}			6×10^{-10}			2×10^{-9}			6.5×10^{-6}		
	56	23	21	72	15	13	89	1	10	83	16	0	1
700		7×10^{-11}			2×10^{-10}			2×10^{-10}			1.4×10^{-6}		
	36	43	21	82	12	6	64	28	7	92	8	0	0
1500		2×10^{-11}			4×10^{-11}			3×10^{-11}			4.3×10^{-8}		
	97	2	1	99	1	0	99	1	0	0	100	0	0

[a] Assuming distance of 50 kpc and no interstellar absorption.

TABLE 5

MODEL W7FM K X-RAY FLUXES

TIME (days)	Si (cm^{-2} s^{-1})[a]			S (cm^{-2} s^{-1})[a]			Ca (cm^{-2} s^{-1})[a]			Fe (cm^{-2} s^{-1})[a]			
	Photon	Coll.	Brems.	Photon	Coll.	Brems.	Photon	Coll.	Brems.	e^--Capture	Photon	Coll.	Brems.
20		5×10^{-9}			4×10^{-9}			5×10^{-9}			5.1×10^{-7}		
	11	88	1	16	82	2	28	68	4	63	22	13	2
40		4×10^{-9}			4×10^{-9}			9×10^{-9}			1.6×10^{-6}		
	19	80	1	21	77	3	52	43	4	89	5	5	1
80		4×10^{-9}			5×10^{-9}			2×10^{-8}			4.5×10^{-6}		
	27	70	3	46	51	3	72	25	4	95	2	3	1
150		3×10^{-9}			6×10^{-9}			2×10^{-8}			7.6×10^{-6}		
	38	60	1	63	36	1	94	4	2	96	2	2	0

[a] Assuming distance of 1 Mpc and no interstellar absorption.

TABLE 6

MODEL WR6C K X-RAY FLUXES

TIME (days)	Si (cm^{-2} s^{-1})[a]			S (cm^{-2} s^{-1})[a]			Ar (cm^{-2} s^{-1})[a]			Fe (cm^{-2} s^{-1})[a]			
	Photon	Coll.	Brems.	Photon	Coll.	Brems.	Photon	Coll.	Brems.	e^--Capture	Photon	Coll.	Brems.
50		1×10^{-14}			5×10^{-12}			5×10^{-12}			2×10^{-10}		
	77	2	21	100	0	0	98	0	2	0	86	1	14
100		6×10^{-11}			3×10^{-10}			3×10^{-10}			6.0×10^{-8}		
	20	61	18	71	21	8	73	12	15	0	86	2	12
200		9×10^{-11}			1×10^{-10}			6×10^{-11}			9.0×10^{-9}		
	1	89	10	2	76	22	4	62	34	0	38	17	45
300		3×10^{-11}			5×10^{-11}			3×10^{-11}			2.5×10^{-9}		
	0	93	7	14	74	12	0	67	33	0	9	31	60

[a] Assuming distance of 1 Mpc and no interstellar absorption.

TABLE 7

MODEL WR6CFM K X-RAY FLUXES

TIME (days)	Si (cm^{-2} s^{-1})[a]			S (cm^{-2} s^{-1})[a]			Ar (cm^{-2} s^{-1})[a]			Fe (cm^{-2} s^{-1})[a]			
	Photon	Coll.	Brems.	Photon	Coll.	Brems.	Photon	Coll.	Brems.	e^--Capture	Photon	Coll.	Brems.
50		2×10^{-10}			5×10^{-10}			5×10^{-10}			4×10^{-7}		
	91	3	6	94	2	4	96	1	3	98	1	0	0
100		2×10^{-9}			2×10^{-9}			1×10^{-9}			1.5×10^{-6}		
	26	73	1	47	52	1	80	19	1	99	1	0	0
200		1×10^{-9}			3×10^{-9}			2×10^{-9}			2.2×10^{-6}		
	62	37	1	81	18	1	93	6	1	100	0	0	0
300		8×10^{-10}			2×10^{-9}			2×10^{-9}			1.8×10^{-6}		
	62	37	1	81	18	1	95	4	0	100	0	0	0

[a] Assuming distance of 1 Mpc and no interstellar absorption.

The code records the contribution of each energy deposition mechanism to the ionization rate of atomic K shells. Our calculations show that for heavy elements (heavier than Si), most K-shell vacancies primarily result from photoelectric absorption of Comptonized gammas, while for light atoms (lighter than Si), most K-shell vacancies are due to collisions with Compton electrons. The ratios of Compton scattering, electron collision, and bremsstrahlung K ionization to that of photoelectric absorption of Comptonized gammas increase with decreasing atomic number. The relative rates of photoelectric absorption and other K-ionization processes in heavy elements depend on the amount of intermediate and lighter elements. The photoelectric absorption dominance of the heavy-element K-vacancy rate is even greater in intermediate-element or light-element envelopes. We also find that bremsstrahlung photons can account for up to 10% of heavy element K-shell ionization.

All K-shell vacancy rates decrease with radius and decay with time. Our calculations of K-shell vacancy rates for models W10hmm and SN11E1 (both progressively mixed) fail to show the increase of ionization rate of any element between days 76 and 135 as suggested by Elias et al. (1988) and Graham (1988) in explaining the increase in strength of He I 1.083 μm of SN 1987A observation between days 76 and 135. Perhaps the increase is due instead to the thinning of the envelope accompanied by increase of its surface area. For a uniform density sphere, the mass of the optically thin region increases as t^2, or $\sim(135/76)^2$, and this is considerably larger than the decrease of ionization rate which is about $\sim e^{-76+135/113.6}$. The increase of ionization rate due to the leak of gamma rays from the core into the outer envelope is also not observed after day 50 in model WR6C where most of ^{56}Co is at the center of the core. The increase may occur at earlier time, but not calculated here. On the other hand, our computation does not follow the emission of many lower-energy photons that still have enough energy to ionize He; so the observed increase in the He ionization may be the result of outer-shell electron emission of photons having $h\nu > 25$ eV. Our results for He are therefore incomplete. They show only the relative importance of the high-energy processes.

How much of the K-shell ionization generated within supernovae becomes detectable K X-ray escape? The relative importance of each process of K-shell ionization for different elements and differing types of supernovae is presented in the tables. The contribution of each process to the K X-ray escape depends on both the element and the type of supernova; in general, electron collision is much more important for Type I supernova than for Type II. Electron collision and bremsstrahlung contributions to the K X-ray flux of heavy elements increase with time so that, although their contribution at early times are small, at later times they can be the dominant contributors.

We thank Stan Woosley for detailed listing of his models 10hmm and WR6C, Ken Nomoto for his listings of SN11E1 and W7, and Adam Burrows for his contributions to the Monte Carlo code. We are grateful to Dieter Hartmann for helpful discussions and to Philip Pinto for a constructive review. This research was supported by Naval Research Laboratory Grant N00014-89-J-2034 under the NASA contract for the OSSE Spectrometer DPRS-10987C on *GRO*.

REFERENCES

Arnett, D. W. 1979, ApJ, 230, L37
———. 1980, ApJ, 240, 105
———. 1982, ApJ, 253, 785
Arthurs, A. M., & Moiseiwitsch, B. L. 1958, Proc. R. Soc. Lond. A, 247, 550
Axelrod, T. S. 1980, in Type I Supernovae, ed. J. C. Wheeler (Austin: Univ. Texax Press), 80
Bambynek, W., Crasemann, B., Fink, R. W., Freund, H. U., Mark, H., Swift, C. D., Price, R. E., & Rao, P. V. 1972, Rev. Mod. Phys, 44, 716
Bates, D. R. 1962, Atomic and Molecular Processes (London: Academic)
Brysk, H., & Rose, M. E. 1955, Oak Ridge National Laboratory SP-1830
Burhop, E. H. S. 1940, Proc. Cambridge Phil. Soc., 36, 43
Burrows, A., & The, L.-S. 1990, ApJ, 360, 626
Chevalier, R. A. 1976, ApJ, 207, 872

———. 1981, ApJ, 246, 267
Clayton, D. D., Colgate, S. A., & Fishman, G. 1969, ApJ, 155, 75
Clayton, D. D., & The, L.-S. 1991, ApJ, 375, 221 (CT)
Colgan, S. W. J., & Hollenbach, D. J. 1988, ApJ, 329, L25
Colgate, S. A., Petscheck, A. G., & Kriese, J. T. 1980, ApJ, 237, L81
Eastman, R. G., & Pinto, P. A. 1993, ApJ, 412, 731
Elias, J. H., Gregory, B., Phillips, M. M., Williams, R. E., Graham, J. R., Meikle, W. P. S., Schwartz, R. D., & Wilking, B. 1988, ApJ, 331, L9
Ensman, L. M., & Woosley, S. E. 1988, ApJ, 333, 754
———. 1989, ApJ, 343, 323
Gavrila, M. 1961, Phys. Rev., 124, 1132
Graham, J. R. 1988, ApJ, 335, L53
Hall, H. 1936, Rev. Mod. Phys., 8, 358
ICRU Report 37. 1984, Stopping Powers for Electrons and Positrons (Bethesda: Int. Commission on Radiation Units and Measurements)
Kozma, C., & Fransson, C. 1992, ApJ, 390, 602
Kumagai, S., Shigeyama, T., Nomoto, K., Itoh, M., Nishimura, J., & Tsuruta, S. 1989, ApJ, 345, 412
Lederer, C. M., & Shirley, V. S. 1978, Table of Isotopes (New York: Wiley)
McCray, R., Shull, J. M., & Sutherland, P. 1987, ApJ, 317, L73
Nomoto, K., Shigeyama, T., Kumagai, S., & Hashimoto, M. 1988, Proc. Astron. Soc. Australia, 7, 490
Nomoto, K., Thielemann, F.-K., & Yokoi, K. 1984, ApJ, 286, 644
Pinto, P. A., & Woosley, S. E. 1988a, ApJ, 329, 820
———. 1988b, Nature, 333, 534
Pozdnyakov, L. A., Sobol, I. M., & Sunyaev, R. A. 1983, Ap. Space. Phys. Rev., 2, 189
Rohrlich, F., & Carlson, B. C. 1954, Phys. Rev., 93, 38
Schram, B. L., De Heer, F. J., Van Der Wiel, M. J., & Kistemaker, J. 1965, Physica, 31, 94
Seaton, M. J. 1962, in Atomic and Molecular Processes, ed. D. R. Bates (London: Academic), 374
Smick, A. E., & Kirkpatrick, P. 1945, Phys. Rev., 67, 153
Sobelman, I. I. 1979, Atomic Spectra and Radiative Transitions (Berlin: Springer)
Sutherland, P. G., & Wheeler, J. C. 1984, ApJ, 280, 282
Swartz, D. A. 1991, ApJ, 373, 604
The, L.-S., Burrows, A., & Bussard, R. 1990, ApJ, 352, 731
The, L.-S., Clayton, D. D., & Burrows, A. 1991, in IAU Symp. 143, Wolf-Rayet Stars and Interrelations with Other Massive Stars in Galaxies, ed. K. A. van der Hucht & B. Hidayat (Dordrecht:Kluwer), 357
Wapstra, A. H., Nijgh, G. J., & van Lieshout, R. 1959, Nuclear Spectroscopy (Amsterdam: North-Holland)
Weaver, T. A., Axelrod, T. S., & Woosley, S. E. 1980, in Proc. Texas Workshop on Type I Supernovae, ed. J. C. Wheeler (Austin: Univ. Texas Press), 113
Zombeck, M. V. 1990, Handbook of Space Astronomy and Astrophysics (Cambridge: Cambridge Univ. Press)